

The GHOSDT Simulations: II. Missing Molecules in Simulations of a Self-Regulated Interstellar Medium

ALON GURMAN,¹ CHIA-YU HU (胡家瑜),^{2,3} MICHAEL Y. GRUDIĆ,⁴ ULRICH P. STEINWANDEL,⁴ AND AMIEL STERNBERG^{1,4,5}

¹*School of Physics & Astronomy, Tel Aviv University, Ramat Aviv 69978, Israel*

²*Department of Astronomy, University of Florida, 211 Bryant Space Sciences Center, Gainesville, FL 32611 USA*

³*Institute of Astrophysics and Department of Physics, National Taiwan University, No. 1, Sec. 4, Roosevelt Rd., Taipei 10617, Taiwan*

⁴*Center for Computational Astrophysics, Flatiron Institute, 162 5th Ave, New York, NY 10010, USA*

⁵*Max-Planck-Institut für Extraterrestrische Physik, Giessenbachstrasse 1, D-85748 Garching, Germany*

ABSTRACT

Observations in the Galaxy and nearby spirals have established that the H I-to-H₂ transition at solar metallicity occurs at gas weight of $P_{\text{DE}}/k_B \approx 10^4 \text{ K cm}^{-3}$, similar to solar neighbourhood conditions. Even so, state-of-the-art models of a self-regulated interstellar medium underproduce the molecular fraction ($R_{\text{mol}} \equiv M_{\text{H}_2}/M_{\text{HI}}$) at solar neighbourhood conditions by a factor of $\approx 2 - 4$. We use the GHOSDT suite of simulations at a mass resolution range of $100 - 0.25 M_{\odot}$ (effective spatial resolution range of $\sim 20 - 0.05 \text{ pc}$) run for 500 Myr to show how this problem is affected by modeling choices such as the inclusion of photoionizing radiation, assumed supernova energy, numerical resolution, inclusion of magnetic fields, and including a model for sub-grid clumping. We find that R_{mol} is not converged even at a resolution of $1 M_{\odot}$, with R_{mol} increasing by a factor of 2 when resolution is improved from 10 to $1 M_{\odot}$. Models excluding either photoionization or magnetic fields result in a factor 2 reduction in R_{mol} . The only model that agrees with the observed value of R_{mol} includes our sub-grid clumping model, which enhances R_{mol} by a factor of ~ 3 compared with our fiducial model. This increases the time-averaged R_{mol} to 0.25, in agreement with the Solar circle value, and closer to the observed median value of 0.42 in regions comparable to the solar neighbourhood in nearby spirals. Our findings show that small-scale clumping in the ISM plays a significant role in H₂ formation even in high-resolution numerical simulations.

Keywords: Interstellar medium (847) – Hydrodynamical Simulations (767)

1. INTRODUCTION

Stars form in dense, cold, self-gravitating gas clouds (McKee & Ostriker 2007; Leroy et al. 2008; Tacconi et al. 2020; Chevance et al. 2023). As it cools and condenses, the star-forming interstellar medium (ISM) converts an increasing fraction of its hydrogen gas mass into molecular H₂ form. This conversion, dubbed the H I-to-H₂ transition, is enabled by the attenuation of stellar far-ultraviolet (far-UV) radiation via dust and H₂ self-shielding (Hollenbach et al. 1971; Black & van Dishoeck 1987; Le Petit et al. 2006; Krumholz et al. 2008; Sternberg et al. 2014). In the Galaxy, the H I-to-H₂ transition

has been observed through absorption line spectroscopy (Carruthers 1970; Savage et al. 1977; Gillmon et al. 2006; Rachford et al. 2009) in diffuse gas and 21 cm and CO rotational line emission in dense gas (Wilson et al. 1970; Lee et al. 2012, 2015), showing a steep rise in the H₂ gas surface density at visual extinctions $A_V \sim 0.5$ (with some variation) corresponding to gas surface densities $\sim 10 M_{\odot} \text{ pc}^{-2}$ for solar metallicity. Nakanishi & Sofue (2003, 2006, 2016); Sofue & Nakanishi (2016) mapped out the radial distribution of the H₂ and HI surface densities in the Galaxy. At the Solar circle (galactocentric distance $\approx 8 \text{ kpc}$), they found that R_{mol} , the ratio of H₂ to HI mass, is in the range 0.19–0.26, increasing steeply inwards and towards the galactic central molecular zone. Resolved studies of HI and CO emission of nearby face-on spiral galaxies established correlations between R_{mol}

and other local quantities. [Blitz & Rosolowsky \(2006\)](#) showed that R_{mol} has an almost linear dependence on midplane gas pressure, with significant variation between galaxies. [Leroy et al. \(2008\)](#); [Eibensteiner et al. \(2024\)](#) showed that R_{mol} correlates with gas surface density, midplane gas pressure, stellar mass surface density, and anti-correlates with galactocentric distance. They found typical conditions for the H I-to-H₂ transition to be a gas weight $P_{\text{DE}} \approx 2.3 \times 10^4 \text{ K cm}^{-3}$, gas surface density $\Sigma_{\text{gas}} \approx 14 M_{\odot} \text{ pc}^{-2}$, and stellar mass surface density $\Sigma_{*} \approx 81 M_{\odot} \text{ pc}^{-2}$, all comparable but slightly higher than solar neighbourhood values (Σ_{gas} and Σ_{*} of 10 and $40 M_{\odot} \text{ pc}^{-2}$, respectively).

Modeling the H I-to-H₂ transition has been carried out using 1-dimensional, plane-parallel or spherical photodissociation region (PDR) models with varying levels of complexity ([Tielens & Hollenbach 1985](#); [Black & van Dishoeck 1987](#); [Le Petit et al. 2006](#); [McKee & Krumholz 2010](#); [Sternberg et al. 2014](#)).

In recent years modeling of the star-forming ISM, including the H I-to-H₂ transitions have also been performed using 3-dimensional (magneto-)hydrodynamical simulations. The simulations range from molecular cloud scales (e.g., [Grudić et al. 2021, 2022](#)), where cloud fragmentation and stellar accretion processes are resolved, to simulations of galaxies, either isolated ([Hu et al. 2017, 2019](#); [Steinwandel et al. 2023](#)), or in mergers ([Lahén et al. 2019](#)), or in a cosmological context ([Hopkins et al. 2018](#)).

While providing a more realistic large-scale context for ISM modeling, cosmological simulations must sacrifice spatial resolution and adopt sub-grid recipes to account for the unresolved substructure of the multiphase ISM (the exception being zoom-in simulations of dwarf galaxies, e.g., [Gutcke et al. \(2022\)](#)). Galactic patch simulations (e.g., [Walch et al. 2015](#); [Iffrig & Hennebelle 2015](#); [Kim & Ostriker 2017](#); [Hu et al. 2021](#); [Gurman et al. 2025](#)) aim to model an intermediate spatial scale, with a box size of $\sim \text{kpc}$, spatial resolution of $\lesssim \text{pc}$, and run times of several 100 Myr. Implementation of star formation varies between models, but generally allows for a self-consistent treatment of feedback mechanisms such as supernova (SN) explosions, photoionizing radiation, and stellar winds, thanks to sufficient spatial resolution.

In one of the early versions of the SILCC project [Walch et al. \(2015\)](#) compared $f_{\text{H}_2} = M_{\text{H}_2}/M_{\text{H}}$ in a suite of simulations of solar neighbourhood conditions in a $0.5 \times 0.5 \times 5 \text{ kpc}^3$ volume at 3.9 pc resolution. They included time-dependent thermochemistry, SN feedback, a constant background far-UV radiation field, a treat-

ment for gas- and dust-radiation shielding, and ran their simulations for 100 Myr. By running simulations both with and without self-gravity, varying the SN rate, SN positioning scheme, background far-UV intensity, and inclusion of magnetic fields (see also [Girichidis et al. 2018](#)), they reached instructive conclusions on the effects of different simulation setups on f_{H_2} . They found that self-gravity increased f_{H_2} from ~ 0.1 to ~ 0.4 , and that varying the SN rate from 5 to 45 Myr^{-1} changed f_{H_2} from ~ 0.7 to < 0.1 . [Girichidis et al. \(2018\)](#) found that including magnetic fields led to a decrease in f_{H_2} in the first 60 Myr of simulation time, and that a stronger initial magnetic field lead to lower f_{H_2} , likely due to magnetic pressure delaying disk compression and thus the onset of H₂ formation. Importantly, positioning SNe at the global density peak rather than at random positions reduced f_{H_2} from ~ 0.4 to < 0.05 . The former SN positioning scheme is perhaps more realistic, as SNe are expected to go off in molecular clouds following the death of the first massive stars to form therein. As such, this positioning scheme leads SNe to preferentially affect the pre-existing molecular gas in which they are positioned, thus dramatically reducing f_{H_2} .

In [Gatto et al. \(2017\)](#), the model for SN positioning in SILCC was improved by following the formation and accretion histories of sink particles, which represent star clusters. This allowed for a more self-consistent SN positioning when compared with [Walch et al. \(2015\)](#), but the overall f_{H_2} was found to be sensitive to the choice of density threshold, peaking at ~ 0.2 and 0.5 for a threshold of 10^2 and 10^4 cm^{-3} , respectively. In a more recent iteration of SILCC which includes a model for cosmic-ray propagation and models with varying metallicity, [Brugaletta et al. \(2025\)](#) report $f_{\text{H}_2} = 0.1$ for solar metallicity, when restricted to a distance of 250 pc from the midplane.

[Gong et al. \(2018\)](#); [Gong et al. \(2020\)](#) used the first version of the TIGRESS simulations ([Kim & Ostriker 2017](#)) to study the effects of metallicity and environment on CO-to-H₂ conversion factor X_{CO} . They derived chemical abundances in their simulation in post-processing, which required the choice of a chemical evolution time as input for their integration of the equations of chemical evolution. For a chemical evolution time of 50 Myr, they found a time-averaged value of $\langle f_{\text{H}_2} \rangle = 0.12$. For a chemical evolution time of 5 Myr, perhaps more representative of the dynamical time of the neutral gas in their simulations (see Appendix A in [Hu et al. 2021](#)), they found $f_{\text{H}_2} = 0.05$. The latest version of TIGRESS (TIGRESS-NCR; [Kim et al. 2023](#))

includes on-the-fly calculation of the molecular fraction, but has not reported on findings of f_{H_2} .

Smith et al. (2020) simulated a high-resolution (~ 0.1 pc) galaxy patch by using a multi-stage refinement scheme. They simulated a galaxy-scale ISM structure at low resolution without self-gravity or star formation, and then added more physics while improving resolution and reducing the simulated volume, taking into account the large-scale gravitational potential and feedback from the lower-resolution volume that contains it. They reported a value of $f_{\text{H}_2} = 0.21$ for a single snapshot at their medium refinement level. However, this number included mass in young (age < 4 Myr) sink particles that represent star clusters. At the refinement level for which they reported this value of R_{mol} , the sink formation density threshold was 574 cm^{-3} , and the star formation efficiency at the sink level was assumed to be 0.02, effectively meaning that most of the gas above this density threshold was unaffected by pre-SN feedback. Excluding this gas, f_{H_2} dropped to 0.11.

Hu et al. (2021) simulated a $1 \times 1 \times 20 \text{ kpc}^3$ box at $m_g = 1 M_\odot$ resolution (effective spatial resolution of 0.2 pc), with time-dependent chemistry. In their model, single stars are formed from gas particles according to a Jeans mass threshold and are assigned a mass according to a stochastic sampling from an assumed Kroupa (2002) initial mass function. In turn, this mass determined the photoionizing photon budget of the star and whether it sets off a SN explosion at the end of its life. They also included a global background far-UV field which scales with the instantaneous star formation rate (SFR), and a model for gas- and dust-shielding. They found $R_{\text{mol}} \approx 2\%$.

In addition to modeling the properties of a self-regulated ISM, Galactic patch simulations are also an ideal setup to make predictions for, or attempt to reproduce, emission line properties from cold atomic or molecular gas. They have been successful at reproducing the observed CO-to- H_2 conversion factor (Gong et al. 2018; Gong et al. 2020; Seifried et al. 2020; Hu et al. 2022). At the same time, they have reproduced the relation between [C II] 158 μm line emission $L_{[\text{C II}]}$ and SFR (Franeck et al. 2018; Ebagezio et al. 2022). Even so, Gurman et al. (2024) showed that the predicted ratio of [C II]-to- H_2 conversion factor was low compared with the observed value (see, e.g., Zanella et al. 2018). Combined, these two results provide further evidence for an underproduction of H_2 in galactic patch simulations.

In light of the apparent tension between observations and simulations, in this paper, we demonstrate

the effects of several physical assumptions and model components in ISM modeling on R_{mol} . We use the GHOSDT simulations (Gurman et al. 2025), a suite of high-resolution magnetohydrodynamical simulations with star-by-star treatment of star formation, effective resolution of 0.05 pc (at the threshold for star formation; for our highest resolution runs). We run our models for 500 Myr, which allows us to average out temporal fluctuations in SFR and R_{mol} , and effectively erase the highly ordered and unrealistic initial conditions which dominate the simulation for the first ~ 200 Myr. In Section 2, we present the observations we benchmark our results against. In Section 3, we describe our numerical setup. In Section 4, we present our resulting R_{mol} . In Section 5, we discuss the effects of considering the sub-grid density structure. We summarize our results in Section 6.

2. OBSERVATIONAL REFERENCES – PHANGS-ALMA SAMPLE

We consider observations from the Physics at High Angular resolution in Nearby Galaxies with Atacama Large Millimeter/submillimeter Array survey (PHANGS-ALMA; Leroy et al. 2021a,b; Querejeta et al. 2024; Chiang et al. 2024). We leverage the high-level data products from PHANGS-ALMA introduced in Sun et al. (2022, 2023). These include 1.5 kpc resolution maps of 80 nearby star-forming galaxies of several quantities of interest. Maps of the H_2 surface density Σ_{H_2} are derived from CO(2-1) line emission observed with ALMA. Maps of the HI surface density Σ_{HI} are derived from 21 cm emission gathered from various programs using the Very Large Array (VLA), Australia Telescope Compact Array (ATCA), and others (see Sun et al. 2022, for full list). The stellar mass surface density Σ_\star is derived from Wide-field Infrared Survey Explorer (WISE; Leroy et al. 2019) and Spitzer Space Telescope images (Sheth et al. 2010). Using these quantities and additional assumptions, the published data also includes the total gas weight estimator P_{DE} (see below).

We demonstrate the observed dependence of R_{mol} on the total (atomic+molecular) hydrogen surface density $\Sigma_{\text{H,tot}}$ in the top panel of Figure 1. As the surface density increases, the gas density and the shielding from FUV radiation both increase, leading to an increase in R_{mol} . Due to a dominant contribution to the gravitational potential from the stellar component, the gas pressure is not determined by $\Sigma_{\text{H,tot}}$ alone. Rather, it is determined by a combination of $\Sigma_{\text{H,tot}}$, the stellar (and dark matter) mass surface density, and the gas vertical scale height. We adopt the gas weight estimator P_{DE}

(Ostriker et al. 2010; Sun et al. 2020; Ostriker & Kim 2022) which can be expressed as

$$P_{\text{DE}} = \frac{\pi G}{2} \Sigma_{\text{gas}}^2 + \Sigma_{\text{gas}} \sqrt{2G\rho_*} \sigma_{\text{gas},z}, \quad (1)$$

where Σ_{gas} is the total gas surface density, ρ_* is the mid-plane stellar density, and $\sigma_{\text{gas},z}$ is the velocity dispersion in the direction perpendicular to the disk plane. ρ_* is estimated using Σ_* and a radially varying disk thickness (Kregel et al. 2002; Sun et al. 2020). $\sigma_{\text{gas},z}$ is assumed to be a constant 11 km s^{-1} .

The middle panel of Figure 1 shows R_{mol} as a function of P_{DE} in the PHANGS–ALMA data. We see a similar trend as with $\Sigma_{\text{H,tot}}$. This can be explained by the increased pressure due to increased gas weight leading to higher gas densities, increasing R_{mol} , but also by the expected correlation between the $\Sigma_{\text{H,tot}}$ and P_{DE} (Blitz & Rosolowsky 2006).

To perform a fair comparison for solar neighbourhood conditions, we examine a subset of the PHANGS–ALMA sample which has $\log(\Sigma_{\text{H,tot}}/(M_{\odot} \text{ pc}^{-2})) = 10 \pm 0.1$. The bottom panel of Figure 1 shows R_{mol} as a function of the stellar mass surface density for this subset of the data. We calculate a binned median and interquartile range for the subset, and find its intersection with the solar neighbourhood value of $\Sigma_* = 40 M_{\odot} \text{ pc}^{-2}$. We find that it has a value of $R_{\text{mol}} = 0.40$, and its interquartile range spans $[0.22, 0.73]$. For the purpose of this work, we treat this value as the benchmark we wish to reproduce in our models, which assume the same stellar- and gas surface density¹.

In the analysis that follows, we do not discuss the effects of the potential environmental or temporal variations in the CO-to-H₂ conversion factor α_{CO} (see, e.g., Bolatto et al. 2013; Gong et al. 2020; Hu et al. 2022).

3. NUMERICAL METHODS

Our simulation suite uses the numerical setup of the GHOSDT (Galaxy Hydrodynamical Simulations of a Supernova Driven Turbulent ISM) presented in Gurman et al. (2025) (hereafter G25), an extension of the simulations of Hu et al. (2021) to include magnetic fields and

¹ We note that there is a local minimum in the median observed R_{mol} dependence on $\Sigma_{\text{H,tot}}$ (at $\sim 10 M_{\odot} \text{ pc}^{-2}$) and P_{DE} (at $\sim 10^4 \text{ K cm}^{-3}$). This is likely explained by an observational bias towards CO-bright regions in low surface density lines of sight, which are expected to be faint in CO emission. If this bias is real and present for the parameter space which we investigate, it could mean that the real value of R_{mol} is lower, perhaps closer to the range of 0.19-0.26 observed at the Solar circle.

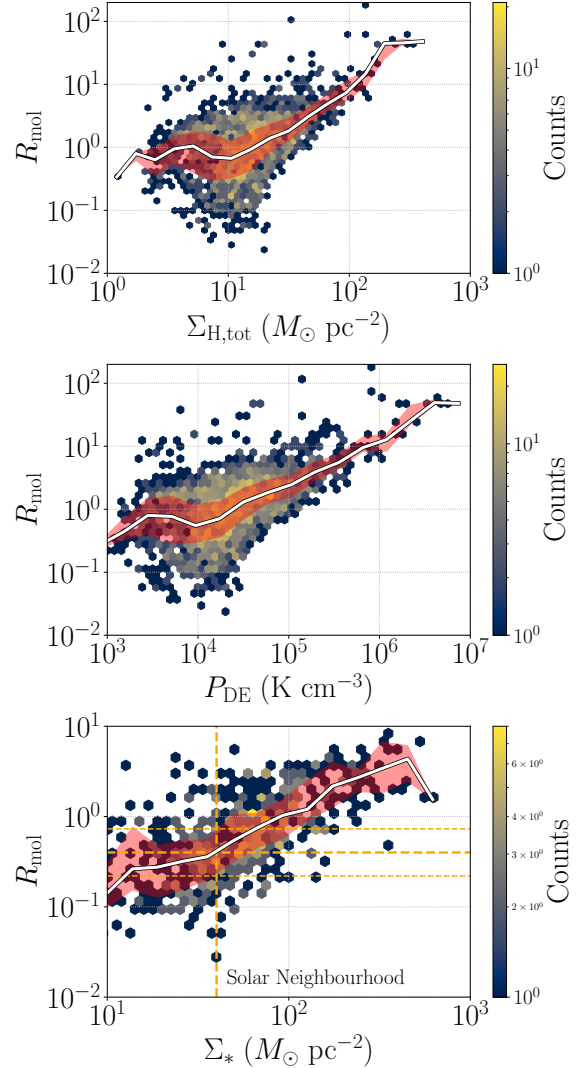


Figure 1. Observational data from the PHANGS–ALMA survey (Leroy et al. 2021a,b; Sun et al. 2022). Top panel: R_{mol} as a function of total hydrogen surface density. Middle panel: R_{mol} as a function of gas weight. Bottom panel: R_{mol} as a function of stellar mass surface density for data with $\log(\Sigma_{\text{H,tot}}/(M_{\odot} \text{ pc}^{-2})) = 1 \pm 0.1$. In all panels, the white line shows the median and the red shaded region shows the 25-75% range.

varying gas surface density. For this work, we consider only models with $\Sigma_{\text{gas}} = 10 M_{\odot} \text{ pc}^{-2}$ and solar metallicity, and vary several modeling choices and parameters as is described in Section 3.4 below.

3.1. Gravity and Magnetohydrodynamics

The GHOSDT simulations are based on the publicly available version of GIZMO (Hopkins 2015), a multimethod code implementing the meshless Godunov-type method (Gaburov & Nitadori 2011) on top of the

TreeSPH code GADGET-3 (Springel 2005). Gravity is solved using the “treecode” method (Barnes & Hut 1986). We treat MHD using the MFM method (Hopkins 2015), and maintain $\nabla \cdot \mathbf{B} \approx 0$ using a combination of 8-wave cleaning (Powell et al. 1999) and the hyperbolic/parabolic divergence cleaning scheme presented in Dedner et al. (2002) following the updates from Tricco & Price (2012) and the (Riemann based) reformulation for the MFM method presented in Hopkins & Raives (2016) (see G25 for more details).

3.2. ISM Physics and Star Formation

Following Hu et al. (2021), we use a cooling and chemistry treatment based on Glover & Mac Low (2007) and Glover & Clark (2012). We include time-dependent treatment of the chemistry of hydrogen species, combined with a HEALPIX (Górski & Hivon 2011) based method to calculate far-UV shielding. This includes shielding by both dust and H_2 from an effective shielding column density for each gas cell.

The model for star formation designates a gas particle as star forming when the local velocity divergence becomes negative and the thermal jeans mass $M_J = (\pi^{2.5} c_s^3) / (6 G^{1.5} \rho^{0.5})$ drops below the kernel mass $M_{\text{ker}} = N_{\text{ngb}} m_g$, where c_s is the sound speed, G is the gravitational constant, ρ is the gas density, m_g is the gas particle mass, and $N_{\text{ngb}} = 32$ is the kernel size. This can be written as a condition on the temperature and density

$$n > 1.4 \times 10^4 \text{ cm}^{-3} \left(\frac{T}{300} \right)^3 \left(\frac{m_g}{M_\odot} \right)^{-2} \left(\frac{\mu}{2.3} \right)^{-3}. \quad (2)$$

This threshold is resolution-dependent by construction, as we expect to resolve higher density gas down to the Jeans scale as our resolution improves. Hu et al. (2021) showed that varying the resolution from 1 to 100 M_\odot has essentially no effect on the time-averaged star formation rate, as it tends to self-regulate through photoionization and SN feedback.

Once a gas particle is considered star-forming, it is assigned a probability of $\epsilon_{\text{sf}} \Delta t / t_{\text{ff}}$ to be converted into a star particle within a single time step, where Δt is the time step, t_{ff} is the local freefall time, and ϵ_{sf} is the star formation efficiency. We set $\epsilon_{\text{sf}} = 0.5$, which is a reasonable choice for a mass resolution of 1 M_\odot , for which the star formation threshold corresponds to a spatial resolution of 0.2 pc. While it might be an inadequate choice to keep ϵ_{sf} constant for models with different resolutions, we choose to do so across all simulations considered in this work for simplicity. In addition to the criteria for

star formation listed above, we enforce an instantaneous star formation density threshold of $n_{\text{isf}} = 10^5 \text{ cm}^{-3}$. Above this density, a gas particle is converted to a star particle instantaneously.

Once formed, a star particle is stochastically assigned a mass by sampling a Kroupa (2002) initial mass function (IMF). This mass is used to determine the photoionizing photon budget of the star and whether it ends its life in a SN explosion, but the star particle inherits the mass of its parent gas particle for the purpose of the gravitational field calculation. As stars form in large numbers in clusters, this method allows us to form stars one by one, predicting the right number of SNe per stars formed without violating mass conservation. If a star is assigned a mass $> 8 M_\odot$, it is designated as a massive star, and we treat its stellar feedback in the form of photoionization and SN explosions following Hu et al. (2017). For each massive star, we determine the position of a quasi-spherical ionization front within which gas temperature is set to 10^4 K and hydrogen is assumed to be fully ionized. The radius of the ionization front is computed iteratively until the total recombination rate in the ionized region matches the mass-dependent ionizing photon budget of the star.

Massive stars also explode as SNe at the end of their mass-dependent lifetime. We model SNe by injecting 10^{51} erg of thermal energy into the 100 nearest neighbours of the star. See G25, Hu (2019), and Steinwandel et al. (2020) for a discussion and justification of applying this model for SN feedback. We do not include a treatment for stellar winds, which can play a role in the evolution of molecular clouds and self-regulation of star formation (see, e.g., Haid et al. 2018; Grudić et al. 2021, 2022; Lancaster et al. 2021a,b).

3.3. Simulation Setup

We simulate an elongated box with a spatial extent of 1 kpc in the x - and y - directions, and 100 kpc in the z direction. Boundary conditions are periodic in x and y , and outflow boundary conditions in z . We define the midplane as $z = 0$, and $z = \pm 50$ kpc as the box boundaries. The initial gas temperature is set to 10^4 K and it is assumed to be entirely in the form of H I. We adopt a constant solar chemical composition with a carbon and oxygen abundance of 1.4×10^{-4} and 3.2×10^{-4} , respectively (Cardelli et al. 1996; Sembach et al. 2000), and a dust-to-gas mass ratio of 0.01. Unless turned off, the initial magnetic field is set to $\mathbf{B} = (5 \mu\text{G}) \hat{x}$ everywhere. The gas initially follows a vertical distribution of the

form

$$\rho(z) = \left(\frac{\Sigma_g}{2H_g} \right) \operatorname{sech}^2 \left(\frac{z}{H_g} \right), \quad (3)$$

where $\Sigma_g = 10 M_\odot \text{ pc}^{-2}$ is the gas surface density and $H_g = 250 \text{ pc}$ is the initial disk scale height. This gives rise to an initial gravitational acceleration of the form

$$a_g = -2\pi G \Sigma_g \tanh \left(\frac{z}{H_g} \right). \quad (4)$$

in the z -direction. Also included is a gravitational potential representing an old stellar population and a dark matter halo, whose dynamics we do not model explicitly. Acceleration due to the stellar component is assumed to take the form

$$a_\star = -2\pi G \Sigma_\star \tanh \left(\frac{z}{H_\star} \right), \quad (5)$$

where $\Sigma_\star = 40 M_\odot \text{ pc}^{-2}$ and $H_\star = 250 \text{ pc}$. The dark matter contribution is due to a Navarro-Frenk-White (Navarro et al. 1997) profile with a virial mass $M_{\text{vir}} = 10^{12} M_\odot$ and concentration parameter $c = 12$. The resulting acceleration is

$$a_{\text{DM}} = -\frac{Gm(r)z}{r^3}, \quad (6)$$

where $r = \sqrt{z^2 + R_0^2}$ represents the radial distance from the center of the halo, and $m(r)$ is the enclosed mass, given by

$$m(r) = 4\pi r_s^3 \rho_s \ln \left[(1 + r/r_s) - (r/r_s) (1 + r/r_s) \right]. \quad (7)$$

In this expression, $r_s = 17 \text{ kpc}$, $\rho_s = 9.5 \times 10^{-3} M_\odot \text{ pc}^{-3}$, and $R_0 = 8 \text{ kpc}$ is the galactocentric distance to the Sun.

3.4. Simulation List

We run a set of variants on the simulations presented in G25. We summarize the list of simulations and their associated names in Table 1. In a first group of simulations, we aim to study the effect of numerical resolution. We run four simulations with the fiducial GHOSDT setup with varying particle mass, ranging from 100 to $0.25 M_\odot$ (named m100 and m0.25, respectively). Assuming $T = 100 \text{ K}$, the corresponding spatial resolution (set by the SPH kernel length) at the density threshold for star formation ranges from 20 pc to 0.05 pc. For our best mass resolution, we scale down the box size in the x - and y - directions to 0.5 kpc in order to conserve computational resources. A second group of simulations is designed to investigate the effect of magnetic fields. We

run pure-hydrodynamical simulations at both 10 and $1 M_\odot$ resolution, labeled H-m10 and H-m1, respectively. The third group is aimed at testing for the effect of potential sub-grid density structure. We expand on this in Section 3.5.

We group together a variety of simulations testing the effect of other parts of our simulation setup, all at $10 M_\odot$ resolution. In NPI-m10 we turn off photoionization feedback. In WSN-m10, we scale down the energy injected per supernova event by a factor of 3, to $3.33 \times 10^{50} \text{ erg}$. L2-m10 has the box size in the x and y directions scaled up to 2 kpc. In LJ-m10 we introduce a variation on our star formation threshold, where we lower the right-hand side of Equation 2 by a factor of 100, to obtain the equivalent Jeans mass threshold for $1 M_\odot$ resolution. While this allows gas to continue to gravitationally collapse to densities for which the Jeans mass is no longer resolved, we use this to complement our resolution study by degrading the mass resolution without changing the star formation prescription. Finally, in HG-m10 we scale up the stellar mass surface density in our external stellar gravitational potential from 40 to $400 M_\odot \text{ pc}^{-2}$. While technically not a solar neighbourhood model, we find it instructive to include this model in our study.

3.5. Model for Unresolved Density Substructure

In models C4-m1 and FC-m1/10/100, we aim to investigate the effect of accounting for unresolved density substructure on R_{mol} . Our approach includes the introduction of a clumping factor, denoted as f_c , to account for the expected increase in the rate of two-body reaction rates in the case of unresolved clumpy structure. This builds on a similar approach implemented by Lupi et al. (2018) in simulations of an isolated galaxy, albeit at lower resolution. The clumping factor is calculated by assuming an unresolved sub-grid log-normal density distribution due to supersonic turbulent motions.

Numerical experiments of artificially driven supersonic turbulence using idealized hydrodynamical simulations (Padoan et al. 1997; Passot & Vázquez-Semadeni 1998) find that the resulting log-normal probability distribution function has a (logarithmic) standard deviation of $1 + (b\mathcal{M})^2$, where \mathcal{M} is the Mach number, and b is a prefactor calibrated numerically. We define the clumping factor

$$f_c \equiv 1 + (b\mathcal{M})^2. \quad (8)$$

In addition, for a log-normal PDF, it follows that

$$f_c = \frac{\langle n^2 \rangle}{\langle n \rangle^2}. \quad (9)$$

Group	Name	m_g (M_\odot)	Description
Resolution Study	m0.25	0.25	Box size scaled down by 2
	m1	1	Fiducial GHOSDT setup
	m10	10	
	m100	100	
Magnetic Fields Off	H-m1	1	
	H-m10	10	
Sub-grid Clumping	C4-m1	1	H ₂ formation artificially scaled up by 4
	FC-m1	1	All 2-body chemical and collisional rates scale with f_c
	FC-m10	10	
	FC-m100	100	
Variations	NPI-m10	10	Photoionization switched off
	WSN-m10		E_{SN} scaled down by 3
	L2-m10		Box size scaled up by 2
	LJ-m10		Modified star formation prescription
	HG-m10		Σ_* scaled up by 10

Table 1. Overview of our suite of simulations.

Equivalently, f_c quantifies the enhancement in two-body reaction rates compared to the constant density case. Federrath et al. (2008) found that $b \approx 1$ for purely compressive forcing, $b \approx 1/3$ for purely solenoidal forcing, and $b \approx 0.5$ for a 50-50 mix of the two. In what follows, we adopt $b = 0.5$. This sub-grid description should not be considered definitive, due to this assumption of constant b , neglect of intermittency, and neglect of physics other than isothermal turbulence. Nevertheless we expect it to model the first-order effect upon the clumping factor: the presence of unresolved structures formed by $\propto \mathcal{M}^2$ isothermal compressions.

We estimate f_c following treatment in the FIRE-3 model (Hopkins et al. 2023). The Mach number is calculated using the ratio of the thermal velocity $v_{\text{therm}} = \sqrt{3k_B T / \mu m_p}$ and the turbulent velocity $v_{\text{turb}} \equiv h |\nabla v|$, where μ is the mean molecular weight, h is the cell size and ∇v is the local velocity gradient. The H₂ abundance weighted average of f_c taken over snapshots in the time range 200-500 Myr of model m-1 is ≈ 4 . This is already an indication that sub-grid clumping is expected to play a non-negligible role in the gas chemistry, an aspect usually ignored in simulations at this resolution. Motivated by this, in model C4-m1, we apply an ad-hoc assumption of $f_c = 4$, and apply it to H₂ formation on dust grains only. Thus, we adjust the formation rate coefficient of

H₂ on dust grains

$$R_{\text{H}_2} = \frac{3.0 \times 10^{-17} \sqrt{T_2}}{1 + 0.4\sqrt{T_2} + 0.15 + 0.2T_2 + 0.08T_2^2} \text{ cm}^{-3} \text{ s}^{-1}, \quad (10)$$

where $T_2 = T/100$ K, up by a factor of 4.

In models FC-m1/10/100, we calculate f_c on the fly and scale up all two-body collisional and chemical reactions in our thermochemistry network in each cell by a factor of f_c . This scaling up of two-body reaction rates is only valid under the assumption that the mixing time for gas within a given cell is shorter than the characteristic timescale for the reactions of interest. We demonstrate the validity of this assumption in Section 5.

4. RESULTS

In Figure 2, we present the time dependence of R_{mol} across our different models. All models show significant temporal fluctuations in R_{mol} . The peaks in R_{mol} correlate with the peaks in SFR due to a large fraction of the gas residing in dense and shielded regions (see, e.g., Gurman et al. 2024). These fluctuations follow the cycle of formation of cold dense gas clouds, gravitational collapse, a rise in SFR, and subsequent heating, ionization, and dispersal of the cloud by stellar feedback. We summarize the time-averaged star formation rates and R_{mol} in panel (f) of Figure 2. With the exception of model HG-m10, the SFR surface density falls within

the range $10^{-3.02}$ to $10^{-2.62} M_{\odot} \text{ yr}^{-1} \text{ kpc}^{-2}$. Given the strong temporal fluctuations in SFR in all of these models, this variation of 0.4 dex can be considered a good agreement between the different models. The elevated SFR in HG-m10 of $10^{-2.19} M_{\odot} \text{ yr}^{-1} \text{ kpc}^{-2}$ is expected as the enhanced background stellar potential increases the gas weight, which is subsequently balanced by increased pressure driven by increased SFR (Ostriker & Kim 2022).

The effect of resolution on R_{mol} is demonstrated in panel (a) of Figure 2. We find an increase in R_{mol} of a factor of 3.3 and 2.5 when varying the resolution from 100 to 10, and from 10 to 1 M_{\odot} , respectively. The change from 1 to 0.25 M_{\odot} is only a factor of 1.2, indicating that we may be approaching convergence. The resolution dependence of R_{mol} is caused by two factors. First, as we increase resolution, we resolve higher-density gas. This is made clear by our Jeans mass threshold for star formation shown in Equation 2. This means that the cold neutral medium (CNM) is not resolved at $m_g = 100 M_{\odot}$, and barely resolved at $m_g = 10 M_{\odot}$. This affects the H_2 mass that resides in the CNM. Even so, R_{mol} in model LJ-m10, which uses the same Jeans mass threshold as m1, agrees with that of model m10. Therefore, it is not our star formation recipe that drives the increase in R_{mol} between models m10 and m1. Instead, this increase is rather due to an improved resolution of the clumpy substructure of the ISM.

Panel (b) of Figure 2 demonstrates the effects of magnetic fields on R_{mol} by comparing MHD and pure-hydrodynamical runs for mass resolution 10 and 1 M_{\odot} . Including magnetic fields leads to an increase in R_{mol} of a factor of 1.5 and 3.5 for 10 and 1 M_{\odot} , respectively. As discussed in G25, magnetic pressure reduces fluctuations in the SFR, while keeping the time-averaged SFR largely unchanged. As a result, the effective disk-height decreases and the cold gas mass fraction increases, which explains the increase in R_{mol} . Even so, R_{mol} in the fiducial solar neighbourhood model m1 still falls short of the observed value by a factor of ~ 4 . Our results are consistent with Hu et al. (2021), who used pure-hydrodynamical simulations and an otherwise identical simulation setup and found that R_{mol} converges at $m_g \leq 10 M_{\odot}$. Since they did not include magnetic fields in any of their models, this suggests that capturing the effect of magnetic fields requires better resolution. It is possible that due to magnetic energy being distributed from small to large scales, the effects of magnetic pressure are sensitive to numerical resolution.

Model HG-m10 shows an increase of a factor of 2.0 in R_{mol} when compared with m10. An increase in R_{mol} is expected when Σ_* increases as the increased background gravitational field drives gas pressure up. Even so, the observational data presented in the bottom panel of Figure 1 suggest a steeper dependence of R_{mol} on Σ_* .

Our experiments with variations on feedback models are shown in panel (d). In WSN-m10, we reduce the energy injected into the ISM per SN event by a factor of 3. This results in an insignificant increase by a factor of 1.15 in R_{mol} when compared with m10. The lower SN energy is still sufficient to disperse molecular clouds, and therefore the effect on the gas conditions is minor. Even so, there is a marginally significant increase in SFR, likely due to a lower turbulent feedback yield when SNe are weakened. In model NPI-m10, where we turn off photoionization feedback, we find a factor of 2.0 reduction in R_{mol} compared with m10. While perhaps counterintuitive at first, this is explained by the fact that photoionization feedback, as our only source of pre-SN feedback, plays an important role in lowering the clustering of SNe, which, in turn, lowers the effectiveness of SNe in disrupting the disk (Smith 2021; Hu et al. 2023).

In panel (e), we present models C4-m1 and FC-m1/10/100. With these models, we attempt to account for unresolved substructure due to supersonic gas motions. In model C4-m1, we scale up the H_2 rate coefficient for formation on dust grains by a factor of 4. This number is the result of computing the clumping factor f_c using Equation 8 for each particle in each snapshot in m1 and taking the H_2 mass-weighted average. Model C4-m1 incorporates a rather ad-hoc modification to our chemical model, and does so inconsistently, as we apply a clumping factor to H_2 formation only rather than to all two-body reactions, both chemical and radiative. In addition, the enhancement in H_2 formation is applied independent of gas density or temperature. Although expected, the result of an increase of a factor of 3.0 is promising as it drives R_{mol} closer to the observed value.

In models FC-m1/10/100, we implement a self-consistent sub-grid model accounting for the unresolved density substructure. Here, f_c is calculated on the fly for each particle and enters our network of cooling and chemical reactions by multiplying the reaction rate of every two-body reaction in our network. The time averaged, H_2 mass-weighted average f_c for models m100, m10, and m1 is 13, 6, and 4, and we find an increase in R_{mol} by a factor of 11.0, 3.97, and 3.0 in models FC-m100, FC-m10, and FC-m1, respectively. Our most promising candidate for explaining the discrepancy

between models and observations is model FC-m1, in which R_{mol} falls within the inter-quartile range of the observed R_{mol} at solar neighbourhood conditions, and in agreement with measurements in the Solar circle. This demonstrates that unresolved substructure is important for H_2 formation in the ISM even at a mass resolution of $1 M_{\odot}$.

5. THE IMPORTANCE OF SUB-GRID STRUCTURE

In this section, we explain how and why accounting for unresolved density substructure affects R_{mol} . The result that R_{mol} increases when scaling up collisional rates by a factor > 1 is expected. The formation of H_2 is dominated by a collisional process scales as n^2 and is locally enhanced by a factor of f_c . H_2 destruction is dominated by photodissociation whose rate does not explicitly depend on the the assumption of unresolved substructure, as the mean density within a gas cell remains unchanged. An indirect effect does enter through the effect on the H_2 shielding column, which will be higher, on average, at a given density when H_2 formation is enhanced. Another effect on shielding, which we do not capture in our sub-grid treatment, is higher porosity of the gas to far-UV radiation.

Most of the H_2 mass to be gained by accounting for sub-grid clumping is from the lower density CNM. Approximately half of the H_2 mass is in the partially molecular, but much more abundant CNM gas with $n \sim 10 - 100 \text{ cm}^{-3}$, as opposed to the fully molecular gas with $n \gtrsim 10^3 \text{ cm}^{-3}$. Figure 3 shows the normalized mass- and H_2 mass-weighted histograms, and the median H_2 abundance as a function of density for models m1 (solid lines) and FC-m1 (dashed lines). While HI in model m1 is fully converted to H_2 only at $n \sim 10^3 \text{ cm}^{-3}$, the wide and prominent peak at lower densities in the mass-weighted histogram leads to 50% of H_2 mass residing in the density range $10\text{-}100 \text{ cm}^{-3}$. When the sub-grid model is applied, the total density PDF does not change drastically, but the molecular abundance at a fixed density does increase significantly. While the H_2 mass in the high-density tail of the PDF does not change much, the increased H_2 abundance in the partially molecular gas drives the large increase in total H_2 mass.

We note that this density range, which is only partially molecular but dominates the H_2 mass budget, is expected to display significant sub-grid clumping. Due to the Lagrangian nature of GIZMO, our spatial resolution of $0.2 \text{ pc} \times (m_g/M_{\odot})^{1/3}$ at $n_{\text{H}} = 1.4 \times 10^4 \text{ cm}^{-3}$

(the typical density for star formation in our m1 model) scales to 2 pc at $n_{\text{H}} \sim 10 \text{ cm}^{-3}$, leading to more unresolved substructure and thus a non-negligible f_c . The top panel of Figure 4 shows the mean sub-grid turbulent velocity as a function of density. We also plot the same curves divided by $(m_g/M_{\odot})^{1/6}$. The curves follow a similar density dependence of roughly $\propto n^{-1/6}$, and once the resolution dependence is factored out agree in value as well. The computed turbulent velocity is also in rough agreement with the Larson (1981) size-linewidth relation, which is $\approx 1 \text{ km s}^{-1}$ at a scale of 1 pc . For $m_g = 1 M_{\odot}$, 1 pc corresponds to $n \approx 13 \text{ cm}^{-3}$, for which we find $v_{\text{turb}} = 2.5 \text{ km s}^{-1}$. At densities above the star formation threshold, which is resolution dependent, the curves diverge. Both the mass resolution and density dependence can be explained to first order under the assumption of $v_{\text{turb}} \propto h^{0.5}$ (Larson 1981) and $h \propto m_g n^{-1/3}$ as holds for Lagrangian codes, where h is the cell radius as represented by the size of the MFM kernel.

The bottom panel of Figure 4 shows the average f_c as a function of density. As the sound speed, shown in the top panel of Figure 4, drops steeply at $n \sim 5 \text{ cm}^{-3}$ due to the collisional excitation of fine structure transitions, f_c increases. At higher densities, the density dependence of the temperature weakens, and we expect the decrease in v_{turb} to drive f_c to lower values, but this density regime is only marginally resolved in the m0.25 model, where we observe a shallow decline of f_c at the highest densities. Following the same line of thought applied to the resolution dependence of v_{turb} , we can deduce that at a given temperature $\mathcal{M} \propto v_{\text{turb}}$ and therefore

$$f_c - 1 = (b\mathcal{M})^2 \propto m_g^{1/3}. \quad (11)$$

This resolution dependence is demonstrated with the dashed lines in the bottom panel of Figure 4, where instead of f_c we plot

$$\tilde{f}_c \equiv (f_c - 1) \times (m_g/M_{\odot})^{-1/3} + 1, \quad (12)$$

and find a reasonable agreement between the different dashed curves and the m1 curve, indicating that the scaling with resolution is well understood. We note that sub-grid clumping has no effect on the H_2 mass in fully molecular gas where R_{mol} is already close to unity. This analysis shows that at a spatial resolution of $\approx 2 \text{ pc}$ (the spatial resolution of our $m_g = 1 M_{\odot}$ models at $n = 10 \text{ cm}^{-3}$) there is sufficient unresolved substructure which requires sub-grid modeling in order to capture H_2 formation correctly.

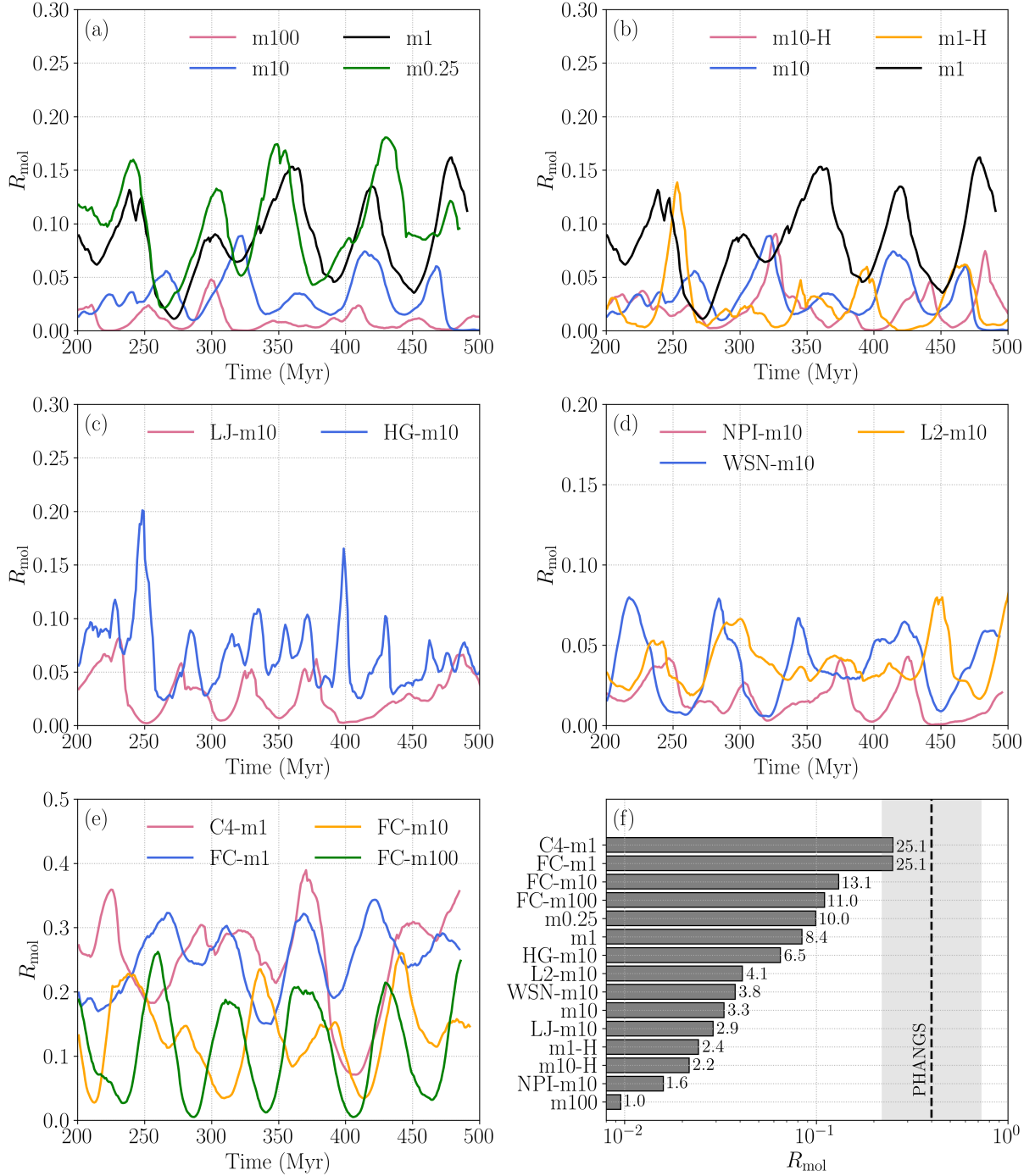


Figure 2. (a)-(e): The H₂-to-HI mass ratio R_{mol} as a function of time for different simulation groups. (a): Resolution study. (b): Effect of magnetic fields. (c)-(d): Variations to feedback and simulations setup. (e): Effects of our clumping sub-grid model. (f): Time averaged values of R_{mol} for all simulations. Vertical dashed line and shaded region show the observed median and interquartile range for PHANGS-ALMA pixels with $\Sigma_{\text{H,tot}} = 10$ and $\Sigma_{\star} = 40 M_{\odot} \text{ pc}^{-2}$. Numbers indicate R_{mol} in % for each model.

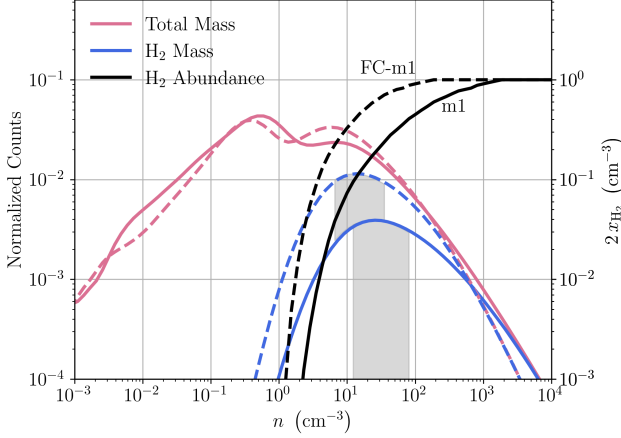


Figure 3. Normalized histogram of the total gas mass (violet) and H₂ mass (blue) in model m1 (solid lines) and FC-m1 (dashed lines). The black solid and dashed lines show the binned median H₂ mass fraction as a function of density for the same models. The shaded regions indicate the density range containing the 25-75% range of H₂ mass in the respective models.

Finally, we address the application of a sub-grid model in a seemingly converged model. In the top panel of Figure 5, we show the time-averaged density histograms of models m100, m10, m1, and m0.25. There seems to be little change in the high-density tail between models m1 and m0.25, consistent with there being a small difference in R_{mol} between the two. Thus, the question arises whether this convergence of the density PDF contradicts the result of $f_c > 1$ and the subsequent increase in R_{mol} when it is applied. To further challenge this, we demonstrate the density histogram of a single snapshot from model m1 alongside the expected density histogram if the sub-grid clumping were resolved. We compute this by drawing 10 new particles for each particle in the snapshot output. We draw these particles from a density PDF corresponding to the computed f_c of each particle and reconstruct the density histogram, after having essentially sampled the sub-grid structure of unresolved gas cells. The new density histogram is not significantly different from that of the original snapshot. The overall shape of the distribution is maintained, no large amount of gas is moved from low-density bins to higher ones, and only a small mass of gas is added at the high-density tail, which constitutes only a small fraction of the total H₂ mass. We also break the resampled density histogram into several components, which originate in particles within density bins with a width of 1 dex. It is clear that while the $\log(n/\text{cm}^{-3}) = 1-10$ bin obtains a high-density tail, the mass in that tail is completely

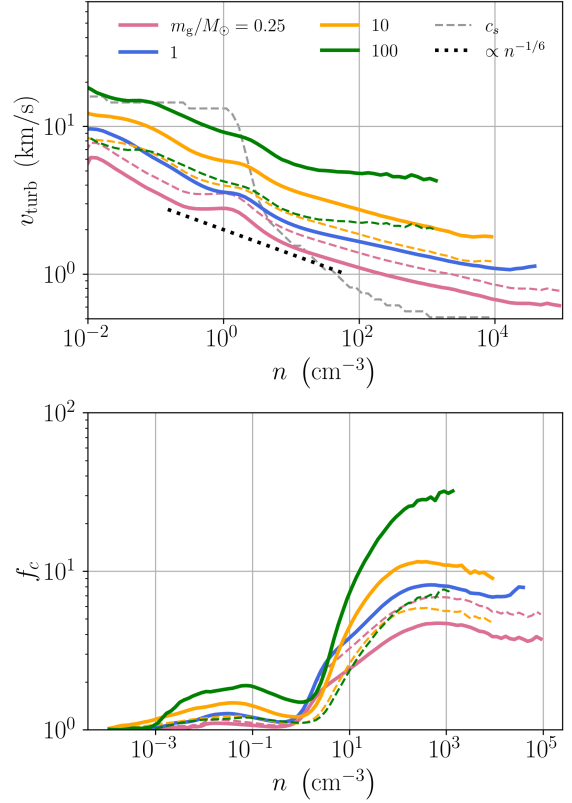


Figure 4. Top panel: v_{turb} as a function of density for models m100, m10, m1, and m0.25. Dashed colored lines show the corresponding solid curves scaled by $(m_g/M_\odot)^{-1/6}$. Also shown is the sound speed for m1, which is essentially independent of resolution, and a power law of the form $n^{-1/6}$ for reference. Bottom panel: as top but for f_c . The dashed lines show the solid curves scaled according to Equation 12.

negligible compared with the total mass in the snapshot in that density range.

Considering the aforementioned analysis, we note that the application of our sub-grid clumping model accounts for an enhancement in $\langle n^2 \rangle$ irrespective of actually adding any dense gas. Rather, the dense unresolved clumps in which formation is enhanced within a larger gas cell are assumed to mix quickly in with the rest of the density distribution, thus enhancing R_{mol} . Since this enhancement is due to the increase in x_{H_2} in the 10-100 cm^3 gas, it is significant even when the density PDF is converged and the characteristic density for the H1-to-H₂ transition of $\approx 10^{-3} \text{ cm}^{-3}$ is resolved.

For the assumption of fast mixing to hold, the timescale for gas mixing within a given gas cell must be short compared to other relevant timescales, in this case the H₂ formation timescale. We approximate an upper bound on the gas mixing time using the cell crossing

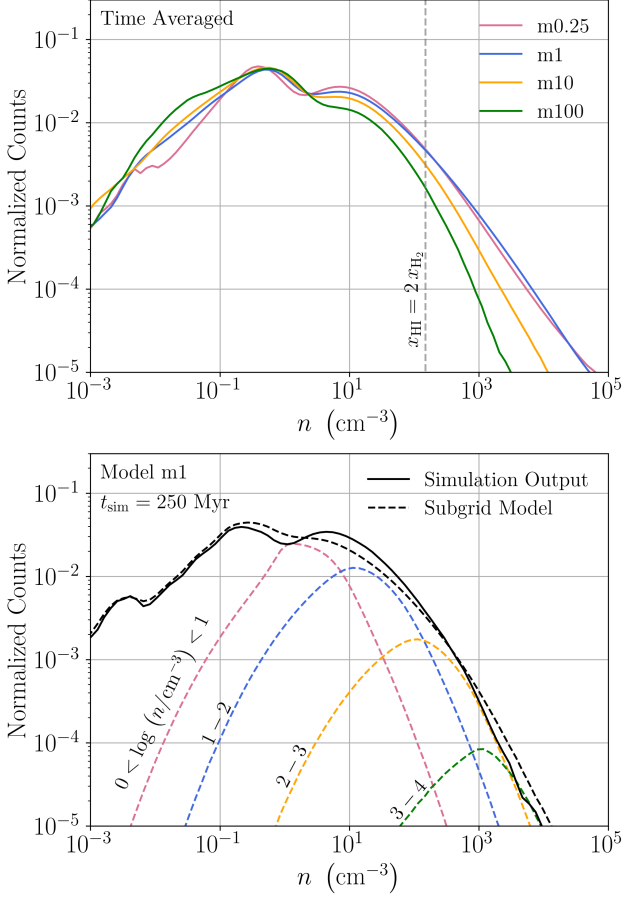


Figure 5. Top panel: normalized mass-weighted density histograms of the total gas mass for simulations in our resolution study, averaged over simulation time 200-500 Myr. The dashed vertical line marks the H I-to-H₂ transition density for our m1 model. Bottom panel: mass-weighted density histogram resulting from our sub-grid model (dashed black; see Section 5), both for model m1. Colored dashed lines show the modified histogram when applied to density bins with a width of 1 dex.

time, i.e., h/v_{turb} where h is the cell size and v_{turb} is the turbulent velocity we describe in Section 3. Using the results shown in Figure 4, we estimate

$$v_{\text{turb}} = 4 \text{ km s}^{-1} (m_g/M_\odot)^{1/6} (n/\text{cm}^{-3})^{-1/6} \quad (13)$$

and the corresponding cell crossing time

$$t_{\text{cross}} = \frac{h}{v_{\text{turb}}} = 1.05 \text{ Myr} (m_g/M_\odot)^{1/6} (n/\text{cm}^{-3})^{-1/6} \quad (14)$$

At the same time, for a temperature of 100 K we can estimate the H₂ formation time

$$t_{\text{H}_2} = \frac{1}{2R_d n} \approx 1.5 \text{ Gyr} (n/\text{cm}^{-3})^{-1}. \quad (15)$$

We thus obtain the ratio of the mixing time and the H₂ formation time

$$\frac{t_{\text{H}_2}}{t_{\text{cross}}} = 1.4 \times 10^3 (n/\text{cm}^{-3})^{-5/6} (m_g/M_\odot)^{-1/6}. \quad (16)$$

For the worst case of $m_g = 100 M_\odot$, we find that $t_{\text{H}_2} = t_{\text{cross}}$ for $n \approx 3000 \text{ cm}^{-3}$. This is above the density at which hydrogen in our simulations is fully converted into molecular form. Therefore, the assumption of rapid mixing is valid for the density range of interest in which $2x_{\text{H}_2} < 1$. We note, however, that other thermochemical processes might be affected by applying our sub-grid model at densities for which the characteristic timescale τ is shorter than the cell crossing time, and a more careful application of the model should be considered, e.g., assuming that $f_c = 1$ for cells where $\tau < t_{\text{cross}}$.

6. SUMMARY

We have presented a set of simulations of a self-regulated, star-forming ISM demonstrating the effect of different modeling choices on the molecular hydrogen fraction R_{mol} . This has been done in light of an apparent discrepancy of a factor of ~ 4 between the observed value of R_{mol} and resolved ISM simulation of $\sim \text{kpc}$ scales. We explored, among other things, the effect of resolution, inclusion of magnetic fields, and a model for unresolved density substructure.

1. Our density PDF and R_{mol} show signs of likely convergence at $m_g = 1 M_\odot$, with a factor of ~ 3 increase in R_{mol} going from 100 to 10 to $1 M_\odot$.
2. Including magnetic fields leads to a factor 3.5 increase in R_{mol} for $m_g = 1 M_\odot$, likely due to a modulation of SFR (G25).
3. Excluding photoionization lowers R_{mol} by a factor of 2 for $m_g = 10 M_\odot$, likely due to more clustered star formation and SN feedback (see Hu et al. 2022).
4. R_{mol} is insensitive to lowering of SN energy by a factor of 3, increasing simulation volume, and varying the star formation Jeans mass threshold.
5. Accounting for sub-grid clumping gives a factor of ~ 3 increase in R_{mol} at $m_g = 1 M_\odot$, due to an enhanced H₂ formation rate in intermediate density gas with $n \sim 10 - 100 \text{ cm}^{-3}$. We point to this model as our most successful effort to relieve the tension between the simulated and observed values of R_{mol} .
6. We compared our predictions for R_{mol} by directly measuring the H₂ content in our simulations, while observations measure Σ_{H_2} indirectly using CO line emission. We point to post processing our simulations to predict CO line luminosity and make a di-

rect comparison with observations as a prospect for further study.

This work highlights the importance of using sufficiently high resolution, including pre-SN feedback and magnetic fields, and accounting for unresolved density substructure (especially in the intermediate density range of $\sim 10 - 100 \text{ cm}^{-3}$) in order to obtain a more realistic R_{mol} . Even so, in our most promising model we still under-predict the observed median value of 0.42 by 40%.

We thank Chris McKee for fruitful discussions. We thank Jiayi Sun for sharing observational data sets. This

work was supported by the German Science Foundation via DFG/DIP grant STE/1869-2 GE 625/17-1, by the National Science and Technology Council (NSTC) of Taiwan under Grant No. NSTC 113-2112-M-002-041-MY3 and National Taiwan University under Grant No. NTU-NFG-114L7444, by the Center for Computational Astrophysics (CCA) of the Flatiron Institute, and the Mathematics and Physical Sciences (MPS) division of the Simons Foundation, USA.

REFERENCES

- Barnes, J., & Hut, P. 1986, *Nature*, 324, 446, doi: [10.1038/324446a0](https://doi.org/10.1038/324446a0)
- Black, J. H., & van Dishoeck, E. F. 1987, *ApJ*, 322, 412, doi: [10.1086/165740](https://doi.org/10.1086/165740)
- Blitz, L., & Rosolowsky, E. 2006, *ApJ*, 650, 933, doi: [10.1086/505417](https://doi.org/10.1086/505417)
- Bolatto, A. D., Wolfire, M., & Leroy, A. K. 2013, *ARA&A*, 51, 207, doi: [10.1146/annurev-astro-082812-140944](https://doi.org/10.1146/annurev-astro-082812-140944)
- Brugaletta, V., Walch, S., Naab, T., et al. 2025, arXiv e-prints, arXiv:2507.08126, doi: [10.48550/arXiv.2507.08126](https://doi.org/10.48550/arXiv.2507.08126)
- Cardelli, J. A., Meyer, D. M., Jura, M., & Savage, B. D. 1996, *ApJ*, 467, 334, doi: [10.1086/177608](https://doi.org/10.1086/177608)
- Carruthers, G. R. 1970, *ApJL*, 161, L81, doi: [10.1086/180575](https://doi.org/10.1086/180575)
- Chevance, M., Krumholz, M. R., McLeod, A. F., et al. 2023, in *Astronomical Society of the Pacific Conference Series*, Vol. 534, *Protostars and Planets VII*, ed. S. Inutsuka, Y. Aikawa, T. Muto, K. Tomida, & M. Tamura, 1, doi: [10.48550/arXiv.2203.09570](https://doi.org/10.48550/arXiv.2203.09570)
- Chiang, I.-D., Sandstrom, K. M., Chasteney, J., et al. 2024, *ApJ*, 964, 18, doi: [10.3847/1538-4357/ad23ed](https://doi.org/10.3847/1538-4357/ad23ed)
- Dedner, A., Kemm, F., Kröner, D., et al. 2002, *Journal of Computational Physics*, 175, 645, doi: [10.1006/jcph.2001.6961](https://doi.org/10.1006/jcph.2001.6961)
- Ebagezio, S., Seifried, D., Walch, S., et al. 2022, arXiv e-prints, arXiv:2206.06393, doi: [10.48550/arXiv.2206.06393](https://doi.org/10.48550/arXiv.2206.06393)
- Eibensteiner, C., Sun, J., Bigiel, F., et al. 2024, *A&A*, 691, A163, doi: [10.1051/0004-6361/202449944](https://doi.org/10.1051/0004-6361/202449944)
- Federrath, C., Klessen, R. S., & Schmidt, W. 2008, *ApJ*, 688, L79, doi: [10.1086/595280](https://doi.org/10.1086/595280)
- Franeck, A., Walch, S., Seifried, D., et al. 2018, *MNRAS*, 481, 4277, doi: [10.1093/mnras/sty2507](https://doi.org/10.1093/mnras/sty2507)
- Gaburov, E., & Nitadori, K. 2011, *MNRAS*, 414, 129, doi: [10.1111/j.1365-2966.2011.18313.x](https://doi.org/10.1111/j.1365-2966.2011.18313.x)
- Gatto, A., Walch, S., Naab, T., et al. 2017, *MNRAS*, 466, 1903, doi: [10.1093/mnras/stw3209](https://doi.org/10.1093/mnras/stw3209)
- Gillmon, K., Shull, J. M., Tumlinson, J., & Danforth, C. 2006, *ApJ*, 636, 891, doi: [10.1086/498053](https://doi.org/10.1086/498053)
- Girichidis, P., Seifried, D., Naab, T., et al. 2018, *MNRAS*, 480, 3511, doi: [10.1093/mnras/sty2016](https://doi.org/10.1093/mnras/sty2016)
- Glover, S. C. O., & Clark, P. C. 2012, *MNRAS*, 421, 116, doi: [10.1111/j.1365-2966.2011.20260.x](https://doi.org/10.1111/j.1365-2966.2011.20260.x)
- Glover, S. C. O., & Mac Low, M. 2007, *ApJS*, 169, 239, doi: [10.1086/512238](https://doi.org/10.1086/512238)
- Gong, M., Ostriker, E. C., Kim, C.-G., & Kim, J.-G. 2020, *ApJ*, 903, 142, doi: [10.3847/1538-4357/abbdab](https://doi.org/10.3847/1538-4357/abbdab)
- Gong, M., Ostriker, E. C., & Wolfire, M. G. 2018, *ApJ*, 866, 163, doi: [10.3847/1538-4357/aae6c9](https://doi.org/10.3847/1538-4357/aae6c9)
- Górski, K. M., & Hivon, E. 2011, *HEALPix: Hierarchical Equal Area isoLatitude Pixelization of a sphere*, *Astrophysics Source Code Library*, <http://ascl.net/1107.018>
- Grudić, M. Y., Guszejnov, D., Hopkins, P. F., Offner, S. S. R., & Faucher-Giguère, C.-A. 2021, *MNRAS*, 506, 2199, doi: [10.1093/mnras/stab1347](https://doi.org/10.1093/mnras/stab1347)
- Grudić, M. Y., Guszejnov, D., Offner, S. S. R., et al. 2022, *MNRAS*, 512, 216, doi: [10.1093/mnras/stac526](https://doi.org/10.1093/mnras/stac526)
- Gurman, A., Hu, C.-Y., Sternberg, A., & van Dishoeck, E. F. 2024, *ApJ*, 965, 179, doi: [10.3847/1538-4357/ad2eac](https://doi.org/10.3847/1538-4357/ad2eac)
- Gurman, A., Steinwandel, U. P., Hu, C.-Y., & Sternberg, A. 2025, *ApJ*, 984, 142, doi: [10.3847/1538-4357/adc814](https://doi.org/10.3847/1538-4357/adc814)
- Gutcke, T. A., Pakmor, R., Naab, T., & Springel, V. 2022, *MNRAS*, 513, 1372, doi: [10.1093/mnras/stac867](https://doi.org/10.1093/mnras/stac867)
- Haid, S., Walch, S., Seifried, D., et al. 2018, *MNRAS*, 478, 4799, doi: [10.1093/mnras/sty1315](https://doi.org/10.1093/mnras/sty1315)

- Hollenbach, D. J., Werner, M. W., & Salpeter, E. E. 1971, *ApJ*, 163, 165, doi: [10.1086/150755](https://doi.org/10.1086/150755)
- Hopkins, P. F. 2015, *MNRAS*, 450, 53, doi: [10.1093/mnras/stv195](https://doi.org/10.1093/mnras/stv195)
- Hopkins, P. F., & Raives, M. J. 2016, *MNRAS*, 455, 51, doi: [10.1093/mnras/stv2180](https://doi.org/10.1093/mnras/stv2180)
- Hopkins, P. F., Wetzel, A., Kereš, D., et al. 2018, *MNRAS*, 480, 800, doi: [10.1093/mnras/sty1690](https://doi.org/10.1093/mnras/sty1690)
- Hopkins, P. F., Wetzel, A., Wheeler, C., et al. 2023, *MNRAS*, 519, 3154, doi: [10.1093/mnras/stac3489](https://doi.org/10.1093/mnras/stac3489)
- Hu, C.-Y. 2019, *MNRAS*, 483, 3363, doi: [10.1093/mnras/sty3252](https://doi.org/10.1093/mnras/sty3252)
- Hu, C.-Y., Naab, T., Glover, S. C. O., Walch, S., & Clark, P. C. 2017, *MNRAS*, 471, 2151, doi: [10.1093/mnras/stx1773](https://doi.org/10.1093/mnras/stx1773)
- Hu, C.-Y., Schrubba, A., Sternberg, A., & van Dishoeck, E. F. 2022, *ApJ*, 931, 28, doi: [10.3847/1538-4357/ac65fd](https://doi.org/10.3847/1538-4357/ac65fd)
- Hu, C.-Y., Sternberg, A., & van Dishoeck, E. F. 2021, *ApJ*, 920, 44, doi: [10.3847/1538-4357/ac0dbd](https://doi.org/10.3847/1538-4357/ac0dbd)
- Hu, C.-Y., Zhukovska, S., Somerville, R. S., & Naab, T. 2019, *MNRAS*, 487, 3252, doi: [10.1093/mnras/stz1481](https://doi.org/10.1093/mnras/stz1481)
- Hu, C.-Y., Smith, M. C., Teyssier, R., et al. 2023, *ApJ*, 950, 132, doi: [10.3847/1538-4357/acff9e](https://doi.org/10.3847/1538-4357/acff9e)
- Iffrig, O., & Hennebelle, P. 2015, *A&A*, 576, 1, doi: [10.1051/0004-6361/201424556](https://doi.org/10.1051/0004-6361/201424556)
- Kim, C.-G., Kim, J.-G., Gong, M., & Ostriker, E. C. 2023, *ApJ*, 946, 3, doi: [10.3847/1538-4357/acbd3a](https://doi.org/10.3847/1538-4357/acbd3a)
- Kim, C.-G., & Ostriker, E. C. 2017, *ApJ*, 846, 133, doi: [10.3847/1538-4357/aa8599](https://doi.org/10.3847/1538-4357/aa8599)
- Kregel, M., van der Kruit, P. C., & de Grijs, R. 2002, *MNRAS*, 334, 646, doi: [10.1046/j.1365-8711.2002.05556.x](https://doi.org/10.1046/j.1365-8711.2002.05556.x)
- Kroupa, P. 2002, *Sci. (New York, N.Y.)*, 295, 82, doi: [10.1126/science.1067524](https://doi.org/10.1126/science.1067524)
- Krumholz, M. R., McKee, C. F., & Tumlinson, J. 2008, *ApJ*, 689, 865, doi: [10.1086/592490](https://doi.org/10.1086/592490)
- Lahén, N., Naab, T., Johansson, P. H., et al. 2019, *ApJL*, 879, L18, doi: [10.3847/2041-8213/ab2a13](https://doi.org/10.3847/2041-8213/ab2a13)
- Lancaster, L., Ostriker, E. C., Kim, J.-G., & Kim, C.-G. 2021a, *ApJ*, 914, 89, doi: [10.3847/1538-4357/abf8ab](https://doi.org/10.3847/1538-4357/abf8ab)
- . 2021b, *ApJ*, 914, 90, doi: [10.3847/1538-4357/abf8ac](https://doi.org/10.3847/1538-4357/abf8ac)
- Larson, R. B. 1981, *MNRAS*, 194, 809, doi: [10.1093/mnras/194.4.809](https://doi.org/10.1093/mnras/194.4.809)
- Le Petit, F., Nehme, C., Le Bourlot, J., & Roueff, E. 2006, *ApJS*, 164, 506, doi: [10.1086/503252](https://doi.org/10.1086/503252)
- Lee, M.-Y., Stanimirović, S., Murray, C. E., Heiles, C., & Miller, J. 2015, *ApJ*, 809, 56, doi: [10.1088/0004-637X/809/1/56](https://doi.org/10.1088/0004-637X/809/1/56)
- Lee, M.-Y., Stanimirović, S., Douglas, K. A., et al. 2012, *ApJ*, 748, 75, doi: [10.1088/0004-637X/748/2/75](https://doi.org/10.1088/0004-637X/748/2/75)
- Leroy, A. K., Walter, F., Brinks, E., et al. 2008, *AJ*, 136, 2782, doi: [10.1088/0004-6256/136/6/2782](https://doi.org/10.1088/0004-6256/136/6/2782)
- Leroy, A. K., Sandstrom, K. M., Lang, D., et al. 2019, *ApJS*, 244, 24, doi: [10.3847/1538-4365/ab3925](https://doi.org/10.3847/1538-4365/ab3925)
- Leroy, A. K., Schinnerer, E., Hughes, A., et al. 2021a, *ApJS*, 257, 43, doi: [10.3847/1538-4365/ac17f3](https://doi.org/10.3847/1538-4365/ac17f3)
- Leroy, A. K., Hughes, A., Liu, D., et al. 2021b, *ApJS*, 255, 19, doi: [10.3847/1538-4365/abec80](https://doi.org/10.3847/1538-4365/abec80)
- Lupi, A., Bovino, S., Capelo, P. R., Volonteri, M., & Silk, J. 2018, *MNRAS*, 474, 2884, doi: [10.1093/mnras/stx2874](https://doi.org/10.1093/mnras/stx2874)
- McKee, C. F., & Krumholz, M. R. 2010, *ApJ*, 709, 308, doi: [10.1088/0004-637X/709/1/308](https://doi.org/10.1088/0004-637X/709/1/308)
- McKee, C. F., & Ostriker, E. C. 2007, *ARA&A*, 45, 565, doi: [10.1146/annurev.astro.45.051806.110602](https://doi.org/10.1146/annurev.astro.45.051806.110602)
- Nakanishi, H., & Sofue, Y. 2003, *PASJ*, 55, 191, doi: [10.1093/pasj/55.1.191](https://doi.org/10.1093/pasj/55.1.191)
- . 2006, *PASJ*, 58, 847, doi: [10.1093/pasj/58.5.847](https://doi.org/10.1093/pasj/58.5.847)
- . 2016, *PASJ*, 68, 5, doi: [10.1093/pasj/psv108](https://doi.org/10.1093/pasj/psv108)
- Navarro, J. F., Frenk, C. S., & White, S. D. M. 1997, *ApJ*, 490, 493, doi: [10.1086/304888](https://doi.org/10.1086/304888)
- Ostriker, E. C., & Kim, C.-G. 2022, *ApJ*, 936, 137, doi: [10.3847/1538-4357/ac7de2](https://doi.org/10.3847/1538-4357/ac7de2)
- Ostriker, E. C., McKee, C. F., & Leroy, A. K. 2010, *ApJ*, 721, 975, doi: [10.1088/0004-637X/721/2/975](https://doi.org/10.1088/0004-637X/721/2/975)
- Padoan, P., Nordlund, A., & Jones, B. J. T. 1997, *MNRAS*, 288, 145, doi: [10.1093/mnras/288.1.145](https://doi.org/10.1093/mnras/288.1.145)
- Passot, T., & Vázquez-Semadeni, E. 1998, *Phys. Rev. E*, 58, 4501, doi: [10.1103/PhysRevE.58.4501](https://doi.org/10.1103/PhysRevE.58.4501)
- Powell, K. G., Roe, P. L., Linde, T. J., Gombosi, T. I., & De Zeeuw, D. L. 1999, *Journal of Computational Physics*, 154, 284, doi: [10.1006/jcph.1999.6299](https://doi.org/10.1006/jcph.1999.6299)
- Querejeta, M., Leroy, A. K., Meidt, S. E., et al. 2024, *A&A*, 687, A293, doi: [10.1051/0004-6361/202449733](https://doi.org/10.1051/0004-6361/202449733)
- Rachford, B. L., Snow, T. P., Destree, J. D., et al. 2009, *ApJS*, 180, 125, doi: [10.1088/0067-0049/180/1/125](https://doi.org/10.1088/0067-0049/180/1/125)
- Savage, B. D., Drake, J. F., Budich, W., & Bohlin, R. C. 1977, *ApJ*, 216, 291, doi: [10.1086/155471](https://doi.org/10.1086/155471)
- Seifried, D., Haid, S., Walch, S., Borchert, E. M. A., & Bisbas, T. G. 2020, *MNRAS*, 492, 1465, doi: [10.1093/mnras/stz3563](https://doi.org/10.1093/mnras/stz3563)
- Sembach, K. R., Howk, J. C., Ryans, R. S. I., & Keenan, F. P. 2000, *ApJ*, 528, 310, doi: [10.1086/308173](https://doi.org/10.1086/308173)
- Sheth, K., Regan, M., Hinz, J. L., et al. 2010, *PASP*, 122, 1397, doi: [10.1086/657638](https://doi.org/10.1086/657638)
- Smith, M. C. 2021, *MNRAS*, 502, 5417, doi: [10.1093/mnras/stab291](https://doi.org/10.1093/mnras/stab291)
- Smith, R. J., Treß, R. G., Sormani, M. C., et al. 2020, *MNRAS*, 492, 1594, doi: [10.1093/mnras/stz3328](https://doi.org/10.1093/mnras/stz3328)
- Sofue, Y., & Nakanishi, H. 2016, *PASJ*, 68, 63, doi: [10.1093/pasj/psw062](https://doi.org/10.1093/pasj/psw062)

- Springel, V. 2005, MNRAS, 364, 1105,
doi: [10.1111/j.1365-2966.2005.09655.x](https://doi.org/10.1111/j.1365-2966.2005.09655.x)
- Steinwandel, U. P., Bryan, G. L., Somerville, R. S.,
Hayward, C. C., & Burkhardt, B. 2023, MNRAS, 526,
1408, doi: [10.1093/mnras/stad2744](https://doi.org/10.1093/mnras/stad2744)
- Steinwandel, U. P., Moster, B. P., Naab, T., Hu, C.-Y., &
Walch, S. 2020, MNRAS, 495, 1035,
doi: [10.1093/mnras/staa821](https://doi.org/10.1093/mnras/staa821)
- Sternberg, A., Petit, F. L., Roueff, E., & Bourlot, J. L.
2014, ApJS, 790, 10S. <https://arxiv.org/abs/1404.5042>
- Sun, J., Leroy, A. K., Ostriker, E. C., et al. 2020.
<https://arxiv.org/abs/2002.08964>
- Sun, J., Leroy, A. K., Rosolowsky, E., et al. 2022, AJ, 164,
43, doi: [10.3847/1538-3881/ac74bd](https://doi.org/10.3847/1538-3881/ac74bd)
- Sun, J., Leroy, A. K., Ostriker, E. C., et al. 2023, ApJL,
945, L19, doi: [10.3847/2041-8213/acbd9c](https://doi.org/10.3847/2041-8213/acbd9c)
- Tacconi, L. J., Genzel, R., & Sternberg, A. 2020, ARA&A,
58, 157, doi: [10.1146/annurev-astro-082812-141034](https://doi.org/10.1146/annurev-astro-082812-141034)
- Tielens, A. G. G. M., & Hollenbach, D. 1985, ApJ, 291,
722, doi: [10.1086/163111](https://doi.org/10.1086/163111)
- Tricco, T. S., & Price, D. J. 2012, Journal of Computational
Physics, 231, 7214, doi: [10.1016/j.jcp.2012.06.039](https://doi.org/10.1016/j.jcp.2012.06.039)
- Walch, S., Girichidis, P., Naab, T., et al. 2015, MNRAS,
454, 238, doi: [10.1093/mnras/stv1975](https://doi.org/10.1093/mnras/stv1975)
- Wilson, R. W., Jefferts, K. B., & Penzias, A. A. 1970,
ApJL, 161, L43, doi: [10.1086/180567](https://doi.org/10.1086/180567)
- Zanella, A., Daddi, E., Magdis, G., et al. 2018, MNRAS,
481, 1976, doi: [10.1093/mnras/sty2394](https://doi.org/10.1093/mnras/sty2394)